Stellar *s*-process neutron capture cross section of Ce isotopes

R. N. Sahoo [1], M. Paul [1,*] Y. Kashiv [2], M. Tessler,[3,1] M. Friedman [1], S. Halfon,[3] A. Kreisel,[3]
A. Shor,[3] and L. Weissman[3]

[1]*Racah Institute of Physics, The Hebrew University of Jerusalem, Jerusalem 91904, Israel*

[2]*Department of Physics & Astronomy, University of Notre Dame, Notre Dame, Indiana 46556, USA*

[3]*Soreq Nuclear Research Center, Yavne 81800, Israel*

Stellar abundances of cerium are of high current interest based both on observations and theoretical models, especially with regard to the neutron-magic ^{140}Ce isotope. A large discrepancy of *s*-process stellar models relative to cerium abundance observed in globular clusters was highlighted, pointing to possible uncertainties in experimental nuclear reaction rates. In this work, the stellar neutron capture cross section of the stable cerium isotopes ^{136}Ce, ^{138}Ce, ^{140}Ce, and ^{142}Ce, were remeasured. A ^{nat}Ce sample was irradiated with quasi-Maxwellian neutrons at $kT = 34.2$ keV using the ^{7}Li(p, n) reaction. The neutron field with an intensity of 3–5×10^{10} n/s was produced by irradiating the liquid-lithium target (LiLiT) with a mA proton beam at an energy (1.92 MeV) just above the threshold at Soreq Applied Research Accelerator Facility (SARAF). The activities of the ^{nat}Ce neutron capture products were measured using a shielded high purity germanium detector. Cross sections were extracted relative to that of the ^{197}Au(n, γ) reaction and the Maxwellian-averaged cross section (MACS) of the Ce isotopes were derived. The MACS values extracted from this experiment are generally consistent with previous measurements and show for ^{140}Ce a value $\approx 15\%$ smaller than most recent experimental values.

I. INTRODUCTION

The four stable isotopes of cerium ($Z = 58$, Fig. 1) display a showcase of processes responsible for production of heavy elements. Since Cameron [1] and Burbidge *et al.* [2], neutron captures are considered the main production gateways for these nuclides via the slow (*s*) and the rapid (*r*) processes while very few proton-rich nuclides (two of those being Ce isotopes) belong to the so-called *p* process. About half of the isotopes of the heavy elements ($A \gtrsim 60$) are produced by the slow (*s*) process. There, the time between consecutive neutron captures is long with respect to typical β^--decay lifetimes along its path, resulting in an evolution close to the valley of stability. The *s* process is further divided into weak and main components. The weak *s* process [3] operates in massive stars, $M_\star > 8M_\odot$, before they explode as type II supernovae and produces nuclides in the mass range $60 \lesssim A \lesssim 90$. The main component [3,4], which produces nuclides in the range $90 \lesssim A \leqslant 209$, takes place in low-mass asymptotic giant branch (AGB) stars, $M_\star \leqslant 4M_\odot$. It operates on a timescale of a few 10^5 years. In a simplified view, most of the neutron exposure experienced by seed nuclei is generated by the ^{13}C$(\alpha, n)^{16}$O neutron source reaction, operating in pulses of a few 10^4 years. The reaction is activated at $T \approx 0.9 \times 10^8$ K (≈ 8 keV) and generates a low neutron number density of $N_n = 10^6$–10^8 cm^{-3}. At the end of such a pulse when the temperature reaches $T \approx 2.5 \times 10^8$ K (≈ 22 keV), a much shorter pulse is activated for a few years during which the ^{22}Ne$(\alpha, n)^{25}$Mg is the main neutron source. It generates a higher neutron number density of $N_n \approx 10^{10}$ cm^{-3}. Due to the short time it operates, the latter neutron source accounts for only a small fraction of the total exposure. However, the higher N_n can affect branching points along the main *s*-process path. The other about half of heavy nuclides are produced by the rapid (*r*) process, in which the time between consecutive neutron captures is short with respect to radioisotope β^--decay lifetimes along its path. The *r* process operates on a timescale of 1 sec under explosive conditions characterized by high temperature, $T > 10^9$ K (≈ 90 keV), and high neutron number density, $N_n > 10^{20}$ cm^{-3} [5]. A third neutron capture process, termed the *i* process, was proposed by Ref. [6]. The neutron number density in this process, $N_n = 10^{12}$–10^{16} cm^{-3}, is intermediate between those the of *r* and *s* processes. It is considered to operate in some special cases [6–9]. Potential confirmation of the *i* process comes from the chemical compositions of carbon-enhanced metal-poor (CEMP)-*r/s* stars, enriched in both *r*- and *s*-process elements. In addition to the neutron capture processes described above, the *p* process produces 35 neutron-deficient stable isotopes. It operates in massive stars under explosive conditions by photonuclear reactions, e.g., $(\gamma, \alpha \setminus n \setminus p)$, on preexisting *r* and *s* isotopes [10,11].

Apart from the *p* nuclides ^{136}Ce and ^{138}Ce, Ce is considered a primarily (main) *s*-process element, with a small *r*-process fraction. Ce was indeed observed in *s*-process enhanced stars [12,13], and in the CEMP-*r/s* stars that may exhibit *i*-process composition [7,8,14]. Cerium is however
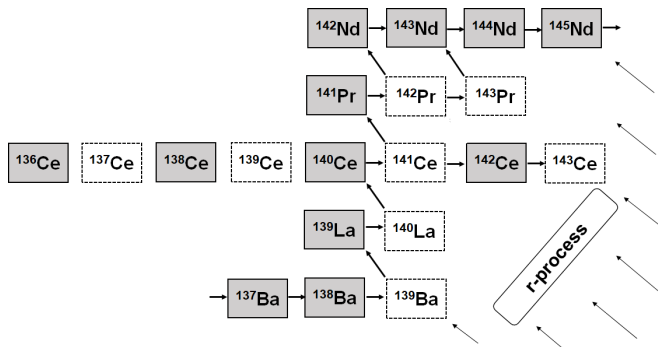
FIG. 1. Part of the nuclide chart showing the *s*-process nucle-osynthesis path in the Ce-Pr-Nd mass around the branching at A = 141–142.
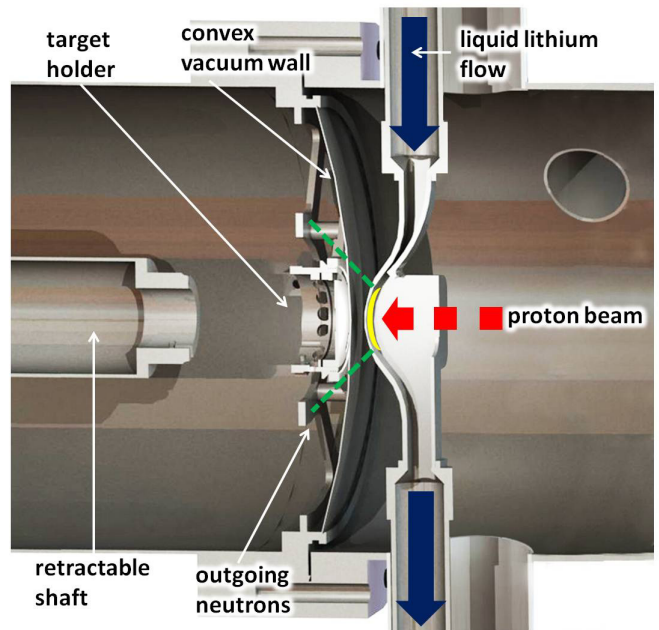

FIG. 2. Cross-section diagram of the liquid-lithium target (LiLiT) and activation target assembly. The proton beam (dashed thick arrow) impinges on the free-surface lithium film; inlet and outlet of the liquid lithium, circulating in a closed loop at $\approx 200\,^\circ$C, are indicated by thick downward arrows (see Ref. [39] for details). The activation target sandwich (Au-Ce-Au) is mounted on a circular target holder and positioned in the outgoing neutron field (dotted lines) at a distance of 6–8 mm from the lithium surface in a vacuum chamber separated from the LiLiT chamber by a 0.5 mm stainless steel wall convex to the beam. The retractable shaft (at left) is used to load and unload rapidly the target assembly.

also observed in *r*-process enhanced stars [15–17] and its presence was reported in the kilonova (AT 2017gfo) following the gravitational wave event GW170817 [18]. A large body of high-quality spectrometric data on the Galactic content of cerium has been recently collected, see, e.g., Ref. [19] and references therein.

For a complete picture of the astronomical data of Ce, one needs to consider presolar grains [20] in addition to abundances in solar and stellar material. Thermodynamic calculations show that Ce is refractory under both C-rich (C/O > 1) conditions [21] and under O-rich (C/O < 1) conditions [22]. The abundance of Ce was measured in single presolar SiC grains (which condense under C-rich conditions) of different subtypes, the source stars of which are believed to be mainly low-mass AGB stars of different metallicities and supernovae [23]. Recently, the Ce abundance was measured for the first time also in a presolar silicate grain (which condense under O-rich conditions), believed to originate in a low-mass AGB star [24]. Also recently, Lugaro *et al.* [25] proposed correlating Ce/Y ratios in Ba stars with ^{88}Sr$/^{86}$Sr ratios in large single presolar SiC grains to infer the type of their source stars.

In this paper we report new measurements of the radiative neutron capture (n, γ) Maxwellian-averaged cross sections (MACS) of the stable isotopes at energies relevant to the *s* and *i* processes; see Refs. [26–28] for previous measurements and a compilation in Ref. [29] and references therein. Of special interest is the (n, γ) reaction on ^{140}Ce, which is a neutron-magic ($N = 82$) nucleus with a typical high neutron binding energy and small neutron capture cross section. ^{140}Ce(n, γ) feeds the potential *s*- and *i*-processes branching point ^{141}Ce (terrestrial $t_{1/2} = 32.504$ d, calculated not to change at *s*- and *i*-process temperatures [30,31]). Koloczek *et al.* [32] calculated that this cross section affects the production of 33 other isotopes in the *s* process. A discrepancy between the Ce abundance observed in the globular clusters M4 [33] and M22 [34] and that calculated by stellar models was recently pointed out by Straniero *et al.* [35] and was attributed possibly to insufficient experimental knowledge of the stellar ^{140}Ce(n, γ) cross section.

The paper is organized as follows. Section II recounts the irradiation of the ^{nat}Ce sample. Section III describes the detection of the activation products by γ spectrometry. Section IV

details the extraction of cross sections. Section V is a short discussion and Sec. VI is a summary. Preliminary results of this experiment were presented in Refs. [36,37].

II. Ce SAMPLE IRRADIATION

The neutron irradiation was performed using the Soreq Applied Research Accelerator Facility (SARAF) and the liquid-lithium target (LiLiT); see Refs. [38,39] for review articles. Quasi-Maxwellian neutrons were produced by an intense proton beam (1–1.5 mA) from the SARAF superconducting linear accelerator bombarding the LiLiT target at an energy of 1.925 MeV, just above the threshold (1881 keV) of the ^{7}Li$(p, n)^7$Be reaction, following the method introduced in Ratynski and Käppeler [40]. The proton beam energy was measured by a Rutherford back-scattering detector located after the accelerator modules, with a typical energy spread of 15 keV. The windowless LiLiT setup (Fig. 2), which consists of liquid lithium (at $\approx 200\,^\circ$C) circulating in closed loop and producing a target film of ≈ 1.5 mm thickness and 18 mm wide, allows for dissipation of the beam power (2–3 kW) by fast transport (2–3 m/s) to a heat exchanger. Neutrons, emitted mostly in the forward direction due to the reaction kinematics, bombarded secondary activation targets located in an experimental chamber at rough vacuum separated by

TABLE I. Areal density (atoms/cm^2) of stable isotopes of cerium in targets Ce-I and Ce-II (see text), and Au(1), Au(2) targets for the above threshold irradiation.

Stable Isotopes ^{nat}Ce, Au	Abundance (%)	Ce-I (atoms/cm^2)	Ce-II (atoms/cm^2)
^{136}Ce	0.185(2)	$3.52(4) \times 10^{18}$	$3.46(4) \times 10^{18}$
^{138}Ce	0.251(2)	$4.63(4) \times 10^{18}$	$4.55(4) \times 10^{18}$
^{140}Ce	88.45(5)	$1.640(1) \times 10^{21}$	$1.612(1) \times 10^{21}$
^{142}Ce	11.11(5)	$2.05(1) \times 10^{20}$	$2.02(1) \times 10^{20}$
^{197}Au(1)	100	6.83×10^{19}	7.24×10^{19}
^{197}Au(2)	100	7.40×10^{19}	7.02×10^{19}

a 0.5 mm thick convex stainless steel wall from the LiLiT chamber and accelerator vacuum. A high-purity metallic ^{nat}Ce target [Ce-I, 25 mm diameter, 2.114(1) g] was sandwiched between two Au foils labeled Au(1) and Au(2) [0.110(1) g and 0.119(1) g, respectively], used as neutron fluence monitors (Table I). Figure 3 illustrates the time profile of the proton current during the irradiation process monitored by a commercial fission detector located in the neutron field at 0° relative to the incident proton beam at ≈80 cm downstream (in air) of the experimental chamber. The time profile was used to calculate a correction for the decay of reaction products during the irradiation, significant for the shortest-lived reaction product ^{137g}Ce ($t_{1/2} = 9$ h). The energy spectrum of the neutron field seen by the target sandwich could not be experimentally determined and was calculated with the aid of the Monte Carlo code SimLiT [41] and the transport code GEANT4 [42] using a detailed model of the LiLiT chamber and target geometry. The SimLiT-GEANT4 codes were carefully benchmarked in previous experiments using the same setup [39,43]. The simulated spectrum of the neutrons subtending the Ce target is shown in Fig. 4 together with a Maxwell-Boltzmann flux distribution
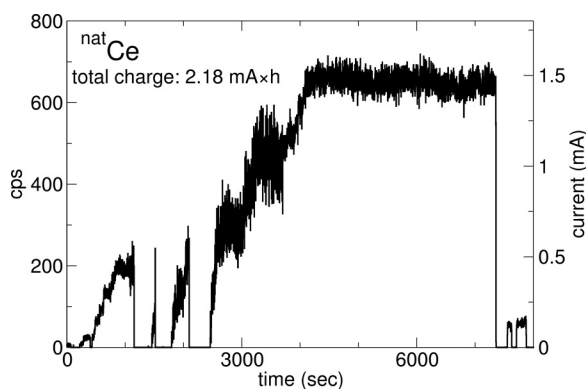

FIG. 3. Time profile of proton beam intensity during irradiation ($E_p = 1.924$ MeV). The left vertical axis represents the count rate of ^{235}U fission events, produced in the fission detector (see text). The right vertical axis displays the corresponding proton beam intensity, calibrated at low intensity against an electron-suppressed Faraday cup located in front of the LiLiT chamber. The low-intensity groups near time = 0 and time = 6750s correspond to the calibration runs of the fission detector. Other gaps are periods of SARAF accelerator instability.
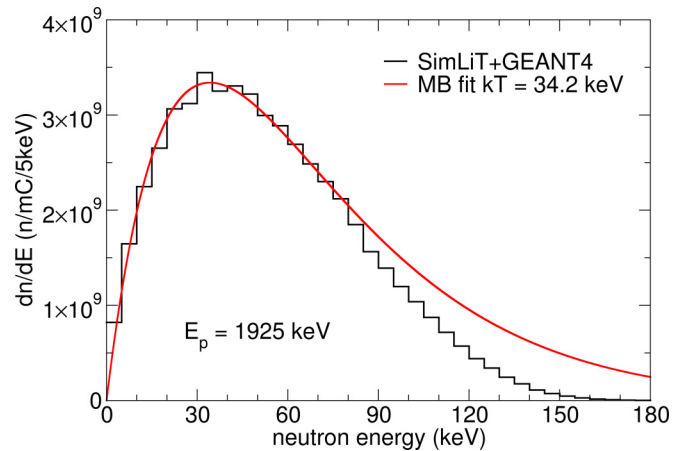

FIG. 4. Simulated neutron spectrum $\frac{dn_{\text{sim}}}{dE_n}$ impinging on the ^{nat}Ce target (histogram) fitted to a Maxwell-Boltzmann flux distribution at 34.2 keV (solid line).

fitted to the simulated spectrum for $T = 34.2$ keV. The simulated experimental spectrum (histogram in Fig. 4) includes 85% of the fitted Maxwell-Boltzmann distribution at $kT = 34.2$ keV The validity of the simulated spectrum is further demonstrated by the fact that the experimental and simulated number of activated Au nuclei [denoted respectively by N_{act}(Au) and $N_{\text{act}}^{\text{ENDF}}$(Au)] [see below Eq. (8)] agree with each other within 1% after normalization to proton charge.

It had been noted in previous experiments [39,43] that in the LiLiT setup using a thick Li target, high-energy γ rays (17.6 and 14.6 MeV) due to the ^{7}Li$(p, \gamma)^8$Be proton capture reaction, produce (γ, n) reactions in the irradiated target, which could interfere with the (n, γ) reaction products. In the present case for example, the ^{140}Ce$(\gamma, n)^{139}$Ce reaction can interfere with the ^{139}Ce production via the ^{138}Ce$(n, \gamma)^{139}$Ce investigated in this work. In order to correct quantitatively for this effect, a separate Ce target (Ce-II, Table I) was irradiated with a pure γ-ray field from the ^{7}Li$(p, \gamma)^8$Be reaction at a proton energy (1.810 MeV) below the neutron threshold (no neutrons present). A Au foil monitored the γ fluence via the ^{197}Au$(\gamma, n)^{196}$Au and ^{196}Au(6.2 d) activity, of well-established cross section. Results of the (n, γ) and (γ, n) irradiations are presented in the next section.

III. DETECTION OF ACTIVATED $^{A+1}$Ce NUCLEI

Detailed information on the identified Ce isotopes, including their half-lives, γ-ray transitions, and intensities are given in Table II. A shielded high purity germanium detector (HPGe) was employed to identify and measure the induced activities of reaction products. Prior to the activity measurement, the detector was calibrated, and its efficiency was determined using a standard multi-γ radioactive source, including ^{22}Na, ^{60}Co, ^{88}Y, ^{133}Ba, ^{137}Cs, ^{241}Am, ^{152}Eu, and ^{155}Eu isotopes, positioned at a distance of 5 cm from the detector end cap. The efficiency curve obtained from this measurement is depicted in Fig. 5. The spectrum of irradiated ^{nat}Ce above (below) neutron threshold, measured at 5 cm distance, is presented in Fig. 6 (Fig. 7), revealing the identification of γ lines cor-

TABLE II. Identified isotopes from ^{nat}Ce(n, γ) reactions, and their half-life, γ-ray transitions, and intensity [44]. Calculated values of the self-absorption coefficient (K_γ) and correction factor f_b, including ^{137m}Ce feeding (see text), are listed.

Identified Isotopes	Half-life	Detected γ-trans (keV)	Intensity (%)	K_γ	f_b
^{137g}Ce	9.11(3) h	447.15(8)	1.68(6)	0.987	0.937
		436.59(9)	0.26(1)	0.985	0.937
^{137m}Ce	34.80(3) h	254.29(5)	11.1(4)	0.966	0.982
^{139}Ce	137.64(2) d	165.86(1)	79.90(13)	0.923	1.000
^{141}Ce	32.51(1) d	145.443(1)	48.30(7)	0.912	0.999
^{143}Ce	33.039(6) h	231.550(2)	2.05(5)	0.957	0.981
		293.226(2)	42.8(4)	0.977	0.981
		350.619(3)	3.23(4)	0.979	0.981
		447.45(2)	0.060(3)	0.977	0.981
		490.368(5)	2.16(3)	0.989	0.981
		664.57(1)	5.69(7)	0.991	0.981
		721.93(1)	5.39(7)	0.992	0.981
		880.46(1)	1.031(13)	0.994	0.981
^{198}Au	2.6941(2) d	411.80	95.62	0.999	0.990

FIG. 7. γ-ray spectrum obtained after irradiating ^{nat}Ce with γ rays from the ^{7}Li(p, γ) reaction (under-threshold energy). Only ^{139}Ce and ^{141}Ce γ transitions are observed and used for correction of the (n, γ) yields. The figure is reproduced from Ref. [37].

responding to ^{137,139,141,143}Ce isotopes and of a metastable state of ^{137}Ce isotope (^{137m}Ce, $t_{1/2} = 34.80$ h, see Fig. 11). Figure 8 represents the γ-ray spectrum of Au(1) (upstream monitor) obtained in above-threshold irradiation. For either irradiation (above or under threshold), the residual number of activated nuclei at time t_{cool} after end of irradiation is obtained using the following equation:

$$n_{act}(t_{cool}) = \frac{C_\gamma(t_{cool})}{\epsilon_\gamma I_\gamma K_\gamma (1 - e^{-\lambda t_{real}})} \frac{t_{real}}{t_{live}} \frac{1}{f_b}; \qquad (1)$$

see decay curves of n_{act} in Figs. 9, 10 for above-threshold and under-threshold irradiation, respectively. In Eq. (1), $C_\gamma(t_{cool})$ is the number of counts in the full-energy peak of a γ line; ϵ_γ, I_γ, and K_γ are the full-energy peak efficiency (Fig. 5), γ-transition intensity and self-absorption coefficient calculated from the target thickness data and the different γ-ray energies, respectively (Table II); λ, t_{real} and t_{live} are the decay constant of the transition, real, and live counting time, respectively. The
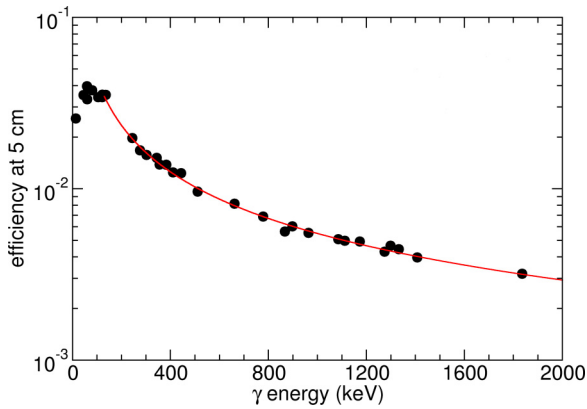

FIG. 5. Full-energy peak efficiency of the HPGe detector using standard multi-γ sources at 5 cm apart from the end cap.
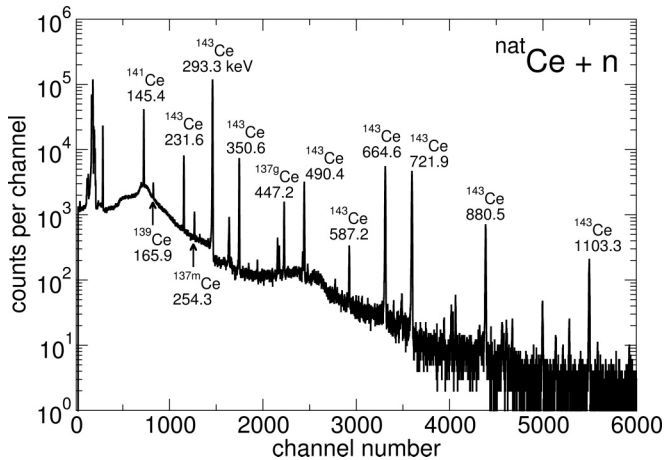

FIG. 6. γ-ray spectrum obtained after irradiating ^{nat}Ce with Maxwellian neutron flux at SARAF-I above threshold energy. γ transition of all the isotopes of ^{nat}Ce(n, γ) reactions are identified along with the isomeric ^{137m}Ce state. The figure is reproduced from Ref. [37].
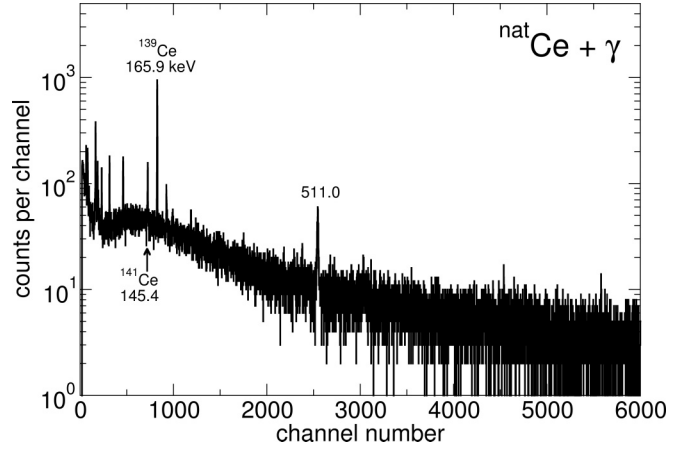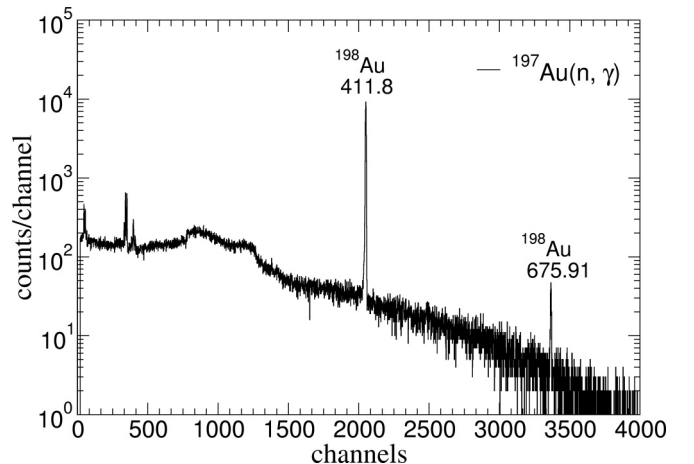

FIG. 8. γ-ray spectrum obtained for the upstream Au(1) monitor (above-threshold irradiation). The ^{198}Au transitions (411.8 keV, and 675.9 keV) are labeled.
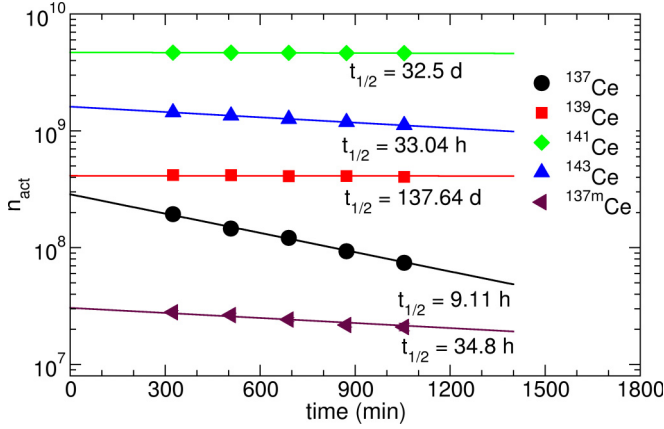
FIG. 9. Decay curves of ^{137,139,141,143}Ce and ^{137m}Ce (irradiation above neutron threshold). Data are fitted using the half-life adopted in the literature.

FIG. 11. Simplified decay scheme of ^{137}Ce, showing the combined decay of $^{137(m+g)}$Ce.

notation f_b refers to a correction for nuclei decaying during the irradiation time, including a minor contribution for ^{137g}Ce due to feeding from the isomeric state ^{137m}Ce, and is explained below. We note here that the 447.2 keV γ transition (Fig. 11), which characterizes the decay of the ^{137}Ce ground state, is practically degenerate with the 447.45 keV (0.06%) transition in ^{143}Ce decay within the resolution of the HPGe detector. In order to correct for this contribution, the counts expected from the 447.45 keV transition were estimated as follows, relative to those of the 293.26 (42.8%) keV γ line in the decay of the same nucleus ^{143}Ce:

$$C_{447.45} = C_{293.26} \frac{I_{447.45}}{I_{293.26}} \frac{\epsilon_{447.45}}{\epsilon_{293.26}} \frac{K_{447.45}}{K_{293.26}}. \qquad (2)$$

C_γ, I_γ, ϵ_γ, and K_γ in Eq. (2) represent the counts, intensity, efficiency of the detector and self-absorption coefficient of the corresponding γ transition, respectively. The contribution of the 447.45 keV transition in ^{143}Ce decay corresponds to $\approx$15% of the full-energy peak observed at this energy and is subtracted from the total peak counts.
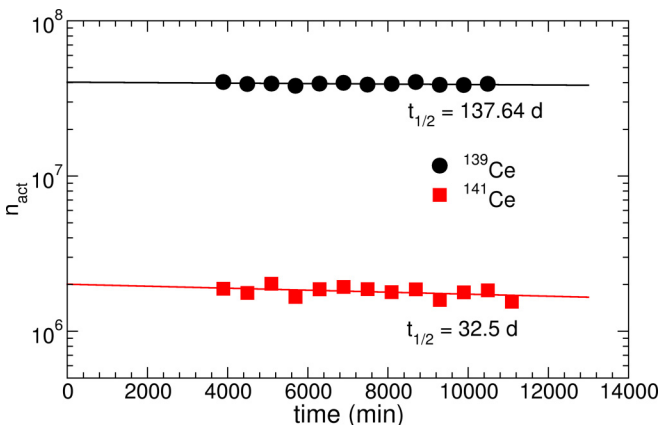

FIG. 10. Decay curves of ^{139,141}Ce (irradiation under neutron threshold). Data are fitted using the half-life adopted in the literature.
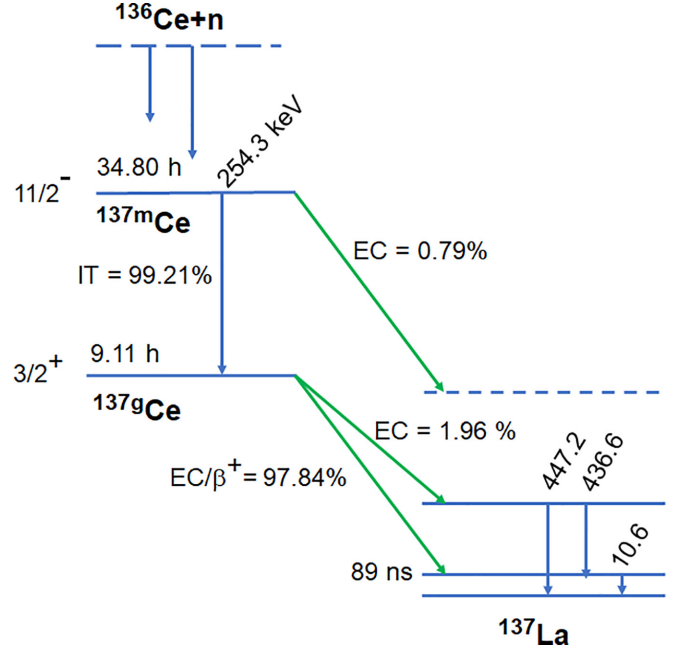
The fraction of activated nuclei decaying during the irradiation time is calculated via the expression

$$f_b = \frac{\int_0^{t_{\text{eoi}}} \Phi_n(t) e^{-\lambda(t_{\text{eoi}} - t)} dt}{\int_0^{t_b} \Phi_n(t) dt}, \qquad (3)$$

where $\Phi_n(t)$ represents the time profile of the neutron intensity on target, taken as proportional to the (neutron-induced) fission chamber yield (e.g., Fig. 6 for above-threshold irradiation). Small additional corrections, overall of the order of 1%, need to be applied in the case of ^{137g}Ce to take into account feeding from the isomeric state ^{137m}Ce (Fig. 11) during irradiation, cooling, and counting; the expressions used for these corrections are given in the Appendix. The final values of f_b are given in Table II.

The number $N_{\text{act}}^{\text{above}}$ ($N_{\text{act}}^{\text{under}}$) of activated ^{A}Ce nuclei produced during the irradiations above (under) neutron threshold (Table III) was extracted from an extrapolation of the respective decay curves to end of irradiation (time = 0, Figs. 9, 10). The net yield N_{act} of the ^{A}Ce(n, γ) reactions was obtained by subtracting the yield produced by (γ, n) reactions during the irradiation above threshold from the measured yield $N_{\text{act}}^{\text{above}}$. The subtracted yield, significant only in the case of the ^{139}Ce product, was obtained from $N_{\text{act}}^{\text{under}}$ after normalization of the respective target thicknesses and incident proton charges (Table III). We note here that the intensity of the high-energy γ rays produced by the ^{7}Li$(p, \gamma)^8$Be reaction, responsible from the (γ, n) yield in our experiment, is dominated by a strong low-energy resonance at $E_R = 441$ keV [45,46]. The difference between the thick-target average cross section for production of high-energy γ rays in the above-threshold ($E_p = 1.912$ MeV) and under-threshold ($E_p = 1.80$ MeV) irradiations is therefore considered negligible.

TABLE III. Number of activated nuclei (N_{act}) obtained in the irradiation above neutron threshold (N_{act}^{above}) and under threshold (N_{act}^{under}) after implementing all corrections. The (γ, n) yield during the above-threshold irradiation [$(\gamma, n)^{above}$] is obtained by normalization of N_{act}^{under} for target thickness and proton charge and is subtracted from N_{act}^{above} to obtain the net yield of (n, γ) reactions (N_{act}). Errors listed are statistical errors only; see Table VII for the overall uncertainty budget.

Reaction Product	$(n, \gamma) + (\gamma, n)$ N_{act}^{above} (10^8)	$(\gamma, n)^{under}$ N_{act}^{under} (10^8)	$(\gamma, n)^{above}$ (10^8)	(n, γ) N_{act} (10^8)
^{137g}Ce	3.04(7)			3.04(7)
^{137m}Ce	0.310(6)			0.310(6)
^{139}Ce	4.14(8)	0.403(2)	1.57(2)	2.57(6)
^{141}Ce	47.0(7)	0.020(1)	0.078(2)	46.96(7)
^{143}Ce	16.43(4)			16.43(4)
^{198}Au(1)	138.8(2)			138.8(2)
^{198}Au(2)	135.5(3)			135.5(3)

IV. ^{A}Ce (n, γ) EXPERIMENTAL CROSS SECTION AND MAXWELLIAN-AVERAGED CROSS SECTIONS

A. Experimental cross sections

The net number of activated ^{A}Ce nuclei N_{act} can be written as

$$N_{act}(x) = \sigma_{expt}(x)\phi_{total}n_t(x), \quad (4)$$

where $\sigma_{expt}(x)$ is our experimental (n, γ) cross section, sometimes termed the spectrum-averaged cross section, ϕ_{total} is the time-integrated neutron rate, and $n_t(x)$ is the areal density of target nuclei x. In our experiment the experimental cross section of cerium isotopes is determined relative to that of ^{197}Au used as monitor in the same irradiation via the equation

$$\sigma_{expt}(x) = \sigma_{expt}(Au)\frac{n_t(Au)N_{act}(x)}{n_t(x)N_{act}(Au)}. \quad (5)$$

The spectrum-averaged cross section $\sigma_{expt}(Au)$ of the ^{197}Au(n, γ) ^{198}Au reaction is calculated via the expression

$$\sigma_{expt}(Au) = \frac{\int \sigma_{ENDF}^{Au}(E_n)\frac{dN_{expt}}{dE_n}dE_n}{\int \frac{dN_{expt}}{dE_n}dE_n}, \quad (6)$$

where the excitation function $\sigma_{ENDF}^{Au}(E_n)$ is taken from the ENDF/B-VIII.0 library [47]. The ENDF/B-VIII.0 library was found to reproduce closely experimental data [48,49] of the ^{197}Au(n, γ) ^{198}Au reaction. The neutron spectrum, $\frac{dN_{expt}}{dE_n}$, is obtained as described in Sec. II from the SimLiT-GEANT4 simulation code [41,50] for each of the Au monitors. The average cross section $\sigma_{expt}(Au)$ for Au(1) is 571.9 mb and for Au(2) is 563.6 mb and the value taken in Eq. (5) is 568(4) mb. The experimental cross sections of the ^{A}Ce isotopes using Eq. (5) and their uncertainty are given in Table IV.

TABLE IV. Experimental neutron capture cross sections (σ_{expt}) of the stable isotopes of Ce.

Reaction	Cross section σ_{expt} (mb)
^{136}Ce(n, γ) ^{137}Ce	262(10)
^{136}Ce(n, γ) ^{137m}Ce	26.7(9)
^{138}Ce(n, γ) ^{139}Ce	163(6)
^{140}Ce(n, γ) ^{141}Ce	8.4(2)
^{142}Ce(n, γ) ^{143}Ce	23.5(9)

B. MACS calculation

The Maxwellian-averaged cross section is defined [40] as,

$$MACS(kT) = \frac{2}{\pi}\frac{\int_0^\infty \sigma(E_n)E_n e^{(-\frac{E_n}{kT})}dE_n}{\int_0^\infty E_n e^{(-\frac{E_n}{kT})}dE_n}, \quad (7)$$

where $\sigma(E_n)$ is the true energy-dependent (n, γ) cross section. Our measurements of the experimental cross sections of Sec. IV A allow us to calibrate evaluated neutron cross-section libraries, corrected to match the measured σ'_{expt}s. Following the method described in Refs. [39,43], the SimLiT-GEANT4 code [41] is used to calculate simultaneously the numbers of (n, γ) activated nuclei for the two gold foils, Au(1) and Au(2), and the Ce target using a neutron capture cross-section library $\sigma_{lib}(E_n)$ and the detailed setup of our experiment. The correction factor C_{lib} for $\sigma_{lib}(E_n)$ is then defined as follows:

$$C_{lib} = \left[\frac{N_{act}(Ce)}{N_{act}(Au)}\right]\bigg/\left[\frac{N_{act}^{lib}(Ce)}{N_{act}^{ENDF}(Au)}\right], \quad (8)$$

where $N_{act}(Ce)$ and N_{act} (Au) are the number of (n, γ) activated Ce isotopes and Au nuclei determined experimentally. N_{act}^{lib} (Ce) and N_{act}^{ENDF}(Au) are, respectively the number of activated Ce isotopes and Au nuclei determined from the SimLiT-GEANT4 simulation using the cross section $\sigma_{lib}(E_n)$ from a given library. The ENDF/B-VIII.0 library was consistently used in the simulation to calculate the number of ^{198}Au activated nuclei N_{act}^{ENDF}(Au). The C_{lib} values derived for several evaluated libraries are given in Table V. Using this definition of C_{lib}, our experimental MACS at temperature T is then determined as

$$MACS_{lib}^{expt}(kT) = \frac{2}{\sqrt{\pi}}\frac{\int_0^\infty C_{lib}\sigma_{lib}(E_n)E_n e^{(-\frac{E_n}{kT})}dE_n}{\int_0^\infty E_n e^{(-\frac{E_n}{kT})}dE_n}, \quad (9)$$

and the extracted values are given in Table VI for $kT = 30$ keV for the respective libraries. Fluctuations in the C_{lib} values

TABLE V. Calculated C_{lib} values (see text) using Eq. (8).

Target nucleus:	^{136}Ce	^{138}Ce	^{140}Ce	^{142}Ce
JENDL-5	1.04	1.23	1.06	1.29
JEFF-3.3	0.97	1.04	1.11	1.29
CENDL-3.2	0.85	3.93	1.06	1.29
ENDF/B-VIII.0	0.85	0.87	1.23	1.33
ROSFOND-10	0.85	0.87	1.23	1.29

TABLE VI. Experimental MACS (mb) at 30 keV using the C_{lib} values and using (n, γ) excitation function from the different libraries and their mean values. The standard deviation, resulting from the use of different values, is taken as representing the uncertainty in the extrapolation of σ_{expt} to a MACS at 30 keV.

Product nucleus:	^{137g}Ce	^{137m}Ce	^{139}Ce	^{141}Ce	^{143}Ce
JENDL-5	291.0	29.7	181.6	9.60	25.80
JEFF-3.3	290.4	29.6	181.5	10.5	25.82
CENDL-3.2	289.3	29.5	185.2	9.61	25.82
ENDF/B-VIII.0	289.3	29.5	181.6	9.59	24.90
ROSFOND	289.3	29.5	181.6	9.59	25.90
Mean (std. dev.)	290.0(8)	29.6(1)	182(2)	9.7(4)	25.8(4)

are observed in Table V, notably for the outlying value of $C_{CENDL}(^{138}$Ce$)$, reflecting different evaluated excitation functions (see Fig. 12) for ^{138}Ce showing an energy dependence of $\sigma_{CENDL}(E_n)$ different from other libraries. Nevertheless, the MACS (30 keV) values listed in Table VI are remarkably stable; the standard deviations are taken as representing the uncertainty in the extrapolation of σ_{expt} to a MACS at 30 keV. Table VII summarizes all uncertainties involved in our experimental MACS values.

Table VIII lists our final value and overall uncertainty of the ^{A}Ce(n, γ) cross section measured for all stable isotopes of cerium along with the isomeric ^{137m}Ce state. The total ^{136}Ce(n, γ) ^{137}Ce (isomeric + ground-state feeding) of astrophysical significance is also listed. Table IX lists the MACS values extrapolated to a larger range of temperatures relevant to different astrophysical sites, using the evaluated library JENDL-5; no uncertainties are assigned for $kT \neq 30$.

V. DISCUSSION

Our results are in general agreement with the previous experimental studies of Kaeppeler *et al.* [26] and Harnood *et al.* [27] with slightly lower uncertainties on the MACS of ^{136}Ce. The MACS value determined at 30 keV for the
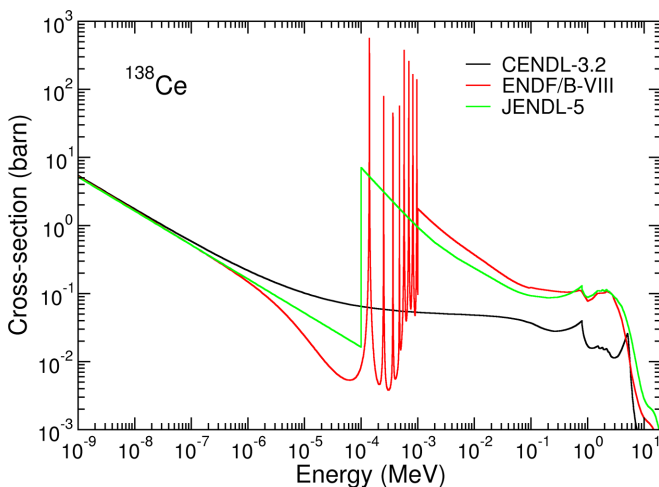

FIG. 12. Comparison of the ^{138}Ce(n, γ) excitation function evaluated in the different libraries.

TABLE VII. List of uncertainties (%) of MACS$_{expt}$ of isotopes ^{nat}Ce.

Source of uncertainty	Uncertainty are in %				
	^{137}Ce	^{137m}Ce	^{138}Ce	^{140}Ce	^{142}Ce
Target thickness	0.4	0.4	0.4	0.4	0.4
Activated nuclei (Ce)	2.0	1.8	2.9	0.2	2.9
Activated nuclei (Au)	0.2	0.2	0.2	0.2	0.2
HPGe efficiency[a]	1.5	1.5	1.5	1.5	1.5
Intensity (I_γ)	0.03	0.03	$\ll 0.01$	$\ll 0.01$	0.01
Simulation[b]	1.8	1.8	1.8	1.8	1.8
σ_{ENDF} (Au)	1.0	1.0	1.0	1.0	1.0
MACS$_{lib}^{expt}$[c]	0.3	0.3	1.2	4.1	1.6
Total uncertainty	3.3	3.2	4.1	4.9	4.2

[a]Systematic error on γ calibration sources.
[b]Includes beam energy, energy spread and geometric positioning of the activation targets.
[c]Standard deviation of MACS values from the different libraries (Table VI).

important case of ^{140}Ce is lower by $\approx 15\%$ than reported in previous experimental studies [26,27] and in the Kadonis database [29]. This lower value partially alleviates the discrepancy highlighted by Straniero *et al.* [35] for cerium in their study of the abundance of heavy elements in globular clusters. We note, however, that the resonance shape analysis done in Ref. [28] for an isolated *p*-wave resonance at $E_n = 5.64$ keV leads to a resonance strength larger than those extracted from the evaluations JENDL-5 and ENDF/B-VIII.0 pointing to a possible conflict with the trend of reduced MACS of ^{140}Ce observed in our experiment.

VI. SUMMARY

We have determined the experimental cross section of neutron capture reactions on the stable isotopes of cerium, averaged over a quasi-Maxwellian neutron spectrum at 34.2 keV. The experiment used the mA proton beam of the SARAF facility incident on the high-power liquid-lithium target (LiLiT). In conjunction with detailed simulations of the experimental system, the experimental cross sections were extrapolated to MACS values at 30 keV and other temperatures relevant to the stellar *s* process. The MACS values obtained for the important

TABLE VIII. Experimental MACS (mb) at 30 keV of stable isotopes of natural cerium from this work compared to values in the literature. Uncertainties include all contributions from Tables III, VI, and VII

Reaction	This work	[26]	[27]	[29]
^{136}Ce(n, γ) ^{137g}Ce	290(11)	300(21)		
^{136}Ce(n, γ) ^{137m}Ce	29.6(10)	28.2(12)		28.2(16)
^{136}Ce$(n, \gamma)^{137(g+m)}$Ce	320(17)			328(21)
^{138}Ce(n, γ) ^{139}Ce	182(8)		179(5)	179(5)
^{140}Ce(n, γ) ^{141}Ce	9.7(5)	11.0(4)	11.5(5)	11.73(44)
^{142}Ce(n, γ) ^{143}Ce	25.8(11)	28.3(10)		29.9(10)

TABLE IX. MACS of stable Ce isotopes in mb between $kT = 10-120$ keV. JENDL-5 library is used to calculate the MACS at different kT values. The MACS are listed according to the product nucleus.

Temp(kT) keV	$^{136g+m}$Ce MACS	^{138}Ce MACS	^{140}Ce MACS	^{142}Ce MACS
10	542	299	14.8	53.9
20	381	215	11.4	32.5
30	320(17)	182(8)	9.7(5)	25.8(11)
40	289	164	8.47	22.6
50	270	153	7.74	20.6
60	258	147	7.26	19.3
70	250	142	6.92	18.4
80	245	139	6.68	17.7
90	240	137	6.51	17.1
100	238	135	6.38	16.7
110	236	134	6.30	16.3
120	234	134	6.25	16.0

neutron-magic nucleus ^{140}Ce is $\approx 15\%$ smaller than previous experimental determinations, partially resolving the discrepancy in the Ce abundance observed in globular cluster stars.

APPENDIX

The ^{137m}Ce isomer decays predominantly (99.2%) by internal transition to the ^{137g}Ce ground state as illustrated in Fig. 11. The additional feeding of the ground state by decay of the isomeric state during irradiation, cooling, and counting time leads to small corrections of the measured yield of ^{137g}Ce decay to obtain its prompt feeding yield from the (n, γ) reaction.

During irradiation, the correction factor f_b^{137g} for ^{137g}Ce production can is expressed by

$$f_b^{137Ce} = f_b + \frac{b_f \sigma_m}{\sigma_g}\left[\frac{(1 - e^{-\lambda_g t_b})}{\lambda_g t_b} - \frac{(e^{-\lambda_m t_b} - e^{-\lambda_g t_b})}{(\lambda_g - \lambda_m)t_i}\right],\tag{A1}$$

where $\lambda_{g,m}$ are the respective decay constants of ^{137g,m}Ce, t_b and b_f the beam irradiation time and the m-to-g branching ratio, respectively. The correction to f_b is of 0.17%.

A fraction of the ^{137m}Ce nuclei produced during irradiation decays to the ground state during the cooling time t_{cool} between end of irradiation and start of counting, given by the following expression:

$$f'_{cool} = f_{cool} + \frac{\sigma_m f_{b,m}}{\sigma_g f_{b,g}}\left[\frac{e^{-\lambda_m t_{cool}} - e^{-\lambda_g t_{cool}}}{\lambda_g - \lambda_m}\right]\lambda_m,\tag{A2}$$

where $f_{cool} = e^{-\lambda_m t_{cool}}$. The correction to the counted ^{137g}Ce decays is of 0.27%.

Similarly, a fraction of the ^{137m}Ce states decays to the ground state during the counting time, expressed by

$$N_{act}^{137g Ce} = N_{act} - \frac{b_f N_m}{\lambda_g - \lambda_m}$$
$$\cdot \left[\frac{\lambda_m(e^{-\lambda_g t_m} - 1) - \lambda_g(e^{-\lambda_m t_m} - 1)}{(1 - e^{-\lambda_m t_m})}\right],\tag{A3}$$

where N_{act} and N_m are the respective number ^{137g}Ce and ^{137m}Ce activated nuclei using Eq. (1) and t_m represents counting time. In each measurement, the contribution of the isomeric state varies between 0.4%–0.7% of the total ^{137g}Ce population. The corrections above are included in the coefficients f_b listed in Table II.

[1] A. G. W. Cameron, Publ. Astron. Soc. Pac. **69**, 201 (1957).

[2] E. M. Burbidge, G. R. Burbidge, W. A. Fowler, and F. Hoyle, Rev. Mod. Phys. **29**, 547 (1957).

[3] F. Käppeler, R. Gallino, S. Bisterzo, and W. Aoki, Rev. Mod. Phys. **83**, 157 (2011).

[4] M. Lugaro, F. Herwig, J. C. Lattanzio, R. Gallino, and O. Straniero, Astrophys. J. **586**, 1305 (2003).

[5] C. Freiburghaus, J. F. Rembges, T. Rauscher, E. Kolbe, F. K. Thielemann, K. L. Kratz, B. Pfeiffer, and J. J. Cowan, Astrophys. J. **516**, 381 (1999).

[6] J. J. Cowan and W. K. Rose, Astrophys. J. **212**, 149 (1977).

[7] P. A. Denissenkov, F. Herwig, P. Woodward, R. Andrassy, M. Pignatari, and S. Jones, Mon. Not. R. Astron. Soc. **488**, 4258 (2019).

[8] A. Choplin, L. Siess, and S. Goriely, Astron. Astrophys. **648**, A119 (2021).

[9] A. Choplin, L. Siess, and S. Goriely, Astron. Astrophys. **667**, A155 (2022).

[10] B. S. Meyer, Annu. Rev. Astron. Astrophys. **32**, 153 (1994).

[11] A. Choplin, S. Goriely, R. Hirschi, N. Tominaga, and G. Meynet, Astron. Astrophys. **661**, A86 (2022).

[12] C. Abia, I. Dominguez, R. Gallino, M. Busso, S. Masera, O. Straniero, P. de Laverny, B. Plez, and J. Isern, Astrophys. J. **579**, 817 (2002).

[13] W. Aoki, S. G. Ryan, J. E. Norris, T. C. Beers, H. Ando, and S. Tsangarides, Astrophys. J. **580**, 1149 (2002).

[14] D. Karinkuzhi, S. Van Eck, S. Goriely, L. Siess, A. Jorissen, T. Merle, A. Escorza, and T. Masseron, Astron. Astrophys. **645**, A61 (2021).

[15] K. Jonsell, P. S. Barklem, B. Gustafsson, N. Christlieb, V. Hill, T. C. Beers, and J. Holmberg, Astron. Astrophys. **451**, 651 (2006).

[16] C. Siqueira Mello, V. Hill, B. Barbuy, M. Spite, F. Spite, T. C. Beers, E. Caffau, P. Bonifacio, R. Cayrel, P. François, H. Schatz, and S. Wanajo, Astron. Astrophys. **565**, A93 (2014).

[17] E. M. Holmbeck, T. C. Beers, I. U. Roederer, V. M. Placco, T. T. Hansen, C. M. Sakari, C. Sneden, C. Liu, Y. S. Lee, J. J. Cowan, and A. Frebel, Astrophys. J. Lett. **859**, L24 (2018).

[18] N. Domoto, M. Tanaka, D. Kato, K. Kawaguchi, K. Hotokezaka, and S. Wanajo, Astrophys. J. **939**, 8 (2022).

[19] G. Contursi, P. de Laverny, A. Recio-Blanco, E. Spitoni, P. A. Palicio, E. Poggio, V. Grisoni, G. Cescutti, F. Matteucci, L. Spina, M. A. Álvarez, G. Kordopatis, C. Ordenovic, I. Oreshina-Slezak, and H. Zhao, Astron. Astrophys. **670**, A106 (2023).

[20] E. Zinner, in *Meteorites and Cosmochemical Processes*, Vol. 1, edited by A. M. Davis (Elsevier, Amsterdam, 2014), pp. 181–213.

[21] K. Lodders and J. B. Fegley, Meteoritics **30**, 661 (1995).

[22] K. Lodders, Astrophys. J. **591**, 1220 (2003).

[23] S. Amari, P. Hoppe, E. Zinner, and R. S. Lewis, Meteoritics **30**, 679 (1995).

[24] J. Leitner and P. Hoppe, in *LPI Contributions*, LPI Contributions, Vol. 2695 (LPI, Houston, 2022), p. 6252.

[25] M. Lugaro, B. Cseh, B. Világos, A. I. Karakas, P. Ventura, F. Dell'Agli, R. Trappitsch, M. Hampel, V. D'Orazi, C. B. Pereira, G. Tagliente, G. M. Szabó, M. Pignatari, U. Battino, A. Tattersall, M. Ek, M. Schönbächler, J. Hron, and L. R. Nittler, Astrophys. J. **898**, 96 (2020).

[26] F. Käppeler, K. A. Toukan, M. Schumann, and A. Mengoni, Phys. Rev. C **53**, 1397 (1996).

[27] S. Harnood, M. Igashira, T. Matsumoto, S. Mizuno, and T. Ohsaki, J. Nucl. Sci. Technol. **37**, 740 (2000).

[28] S. Amaducci, N. Colonna, L. Cosentino, S. Cristallo *et al.*, Universe **7**, 200 (2021).

[29] Karlsruhe astrophysical database of nucleosynthesis in stars (kadonis v1.0).

[30] K. Cosner and J. W. Truran, Astrophys. Space Sci. **78**, 85 (1981).

[31] K. Takahashi and K. Yokoi, At. Data Nucl. Data Tables **36**, 375 (1987).

[32] A. Koloczek, B. Thomas, J. Glorius, R. Plag, M. Pignatari, R. Reifarth, C. Ritter, S. Schmidt, and K. Sonnabend, At. Data Nucl. Data Tables **108**, 1 (2016).

[33] P. A. Young, K. A. Knierman, J. R. Rigby, and D. Arnett, Astrophys. J. **595**, 1114 (2003).

[34] I. U. Roederer, A. F. Marino, and C. Sneden, Astrophys. J. **742**, 37 (2011).

[35] O. Straniero, S. Cristallo, and L. Piersanti, Astrophys. J. **785**, 77 (2014).

[36] R. N. Sahoo, M. Tessler, S. Halfon, D. Kijel, A. Kreisel, P. M. Arik, A. Shor, and L. Weissman, EPJ Web Conf. **279**, 06002 (2023).

[37] M. Tessler, M. Paul, T. Palchan, S. Halfon, L. Weissman, N. Hazenshprung, A. Kreisel, T. Makmal, A. Shor, I. Silverman, M. A. Coronado, S. Almaraz-Calderon, W. Jiang, Z.-T. Lu, P. Mueller, R. Pardo, K. Ernst Rehm, R. Scott, R. Talwar, C. Ugalde *et al.*, PoS (**INPC2016**) 139 (2016).

[38] I. Mardor, O. Aviv, M. Avrigeanu, D. Berkovits, A. Dahan, T. Dickel, I. Eliyahu, M. Gai, I. Gavish-Segev, S. Halfon, M. Hass, T. Hirsh, B. Kaiser, D. Kijel, A. Kreisel, Y. Mishnayot, I. Mukul, B. Ohayon, M. Paul, A. Perry *et al.*, Eur. Phys. J. A **54**, 91 (2018).

[39] M. Paul, M. Tessler, M. Friedman, S. Halfon, T. Palchan, L. Weissman, A. Arenshtam, D. Berkovits, Y. Eisen, I. Eliahu, G. Feinberg, D. Kijel, A. Kreisel, I. Mardor, G. Shimel, A. Shor, and I. Silverman, Eur. Phys. J. A **55**, 44 (2019).

[40] W. Ratynski and F. Käppeler, Phys. Rev. C **37**, 595 (1988).

[41] M. Friedman, D. Cohen, M. Paul, D. Berkovits, Y. Eisen, G. Feinberg, G. Giorginis, S. Halfon, A. Krása, A. Plompen, and A. Shor, Nucl. Instrum. Meth. Phys. Res. A **698**, 117 (2013).

[42] S. Agostinelli *et al.*, Nucl. Instrum. Meth. Phys. Res. A **506**, 250 (2003).

[43] M. Tessler, M. Paul, A. Arenshtam, G. Feinberg, M. Friedman, S. Halfon, D. Kijel, L. Weissman, O. Aviv, D. Berkovits, Y. Eisen, I. Eliyahu, G. Haquin, A. Kreisel, I. Mardor, G. Shimel, A. Shor, I. Silverman, and Z. Yungrais, Phys. Lett. B **751**, 418 (2015).

[44] National Nuclear Data Center, Brookhaven National Laboratory (2023), WWW Document, https://www.nndc.bnl.gov/nudat3/.

[45] D. Zahnow, C. Angulo, C. Rolfs, S. Schmidt, W. H. Schulte, and E. Somorjai, Z. Phys. A **351**, 229 (1995).

[46] M. Munch, O. Sølund Kirsebom, J. A. Swartz, K. Riisager, and H. O. U. Fynbo, Phys. Lett. B **782**, 779 (2018).

[47] D. Brown, M. Chadwick, R. Capote, A. Kahler, A. Trkov, M. Herman, A. Sonzogni, Y. Danon, A. Carlson, M. Dunn, D. Smith, G. Hale, G. Arbanas, R. Arcilla, C. Bates, B. Beck, B. Becker, F. Brown, R. Casperson, J. Conlin *et al.*, Nucl. Data Sheets **148**, 1 (2018).

[48] C. Lederer, N. Colonna, C. Domingo-Pardo, F. Gunsing, Käppeler *et al.*, Phys. Rev. C **83**, 034608 (2011).

[49] C. Massimi, B. Becker, E. Dupont, S. Kopecky, C. Lampoudis, R. Massarczyk, M. Moxon, V. Pronyaev, P. Schillebeeckx, I. Sirakov, and R. Wynants, Eur. Phys. J. A **50**, 124 (2014).

[50] G. Feinberg, M. Friedman, A. Krása, A. Shor, Y. Eisen, D. Berkovits, D. Cohen, G. Giorginis, T. Hirsh, M. Paul, A. J. M. Plompen, and E. Tsuk, Phys. Rev. C **85**, 055810 (2012).